Electrochimica Acta 270 (2018) 417–425

Contents lists available at ScienceDirect

Electrochimica Acta

journal homepage: www.elsevier.com/locate/electacta

# Reduced graphene oxide wrapped $ZnMn_2O_4$/carbon nanofibers for long-life lithium-ion batteries

Qili Gao [b], Zhaoxiao Yuan [a], Linxi Dong [a], Gaofeng Wang [a], Xuebin Yu [b, a, *]

[a] Key Laboratory of RF Circuits and System of Ministry of Education, Electronic and Information College of Hangzhou Dianzi University, Hangzhou 310018, China

[b] Department of Materials Science, Fudan University, Shanghai, China

ARTICLE INFO

*Article history:*
Received 29 January 2018
Received in revised form
16 March 2018
Accepted 18 March 2018
Available online 21 March 2018

*Keywords:*
$ZnMn_2O_4$ nanoparticles
Continuous carbon nanofibers
Reduced graphene oxide
Lithium-ion batteries

ABSTRACT

$ZnMn_2O_4$ is regarded as one of the potential anode materials for lithium-ion batteries (LIBs), due to its high theoretical specific capacity (784 mAh $g^{-1}$). Unfortunately, the bulk $ZnMn_2O_4$ presents an inferior electrochemical performance resulting from the large volume change during the charge-discharge process. In this paper, we report the synthesis and electrochemical properties of $ZnMn_2O_4$ nanoparticles (NPs) that are homogeneously distributed in connective network porous carbon nanofibers wrapped by reduced graphene oxide sheets. The distinctive structure of this composite not only provides enough voids to storage Li-ions and buffer the volume expansion of the $ZnMn_2O_4$ NPs, but also offers a continuous conducting network for Li-ion and electron transportation, resulting in significantly improved electrochemical performances. As binder-free electrodes for LIBs, an optimized $ZnMn_2O_4$@rGO-CNFs sample exhibits a reversible capacity of 1142 mAh $g^{-1}$ at 100 mA $g^{-1}$ over 100 cycles, and a stable capacity of 659 mAh $g^{-1}$ after 1000 cycles at a large current density of 2000 mA $g^{-1}$, enabling $ZnMn_2O_4$ a promising electrode candidate for LIBs.



## 1. Introduction

After the persistent endeavors of scientists towards the increasing energy demand of modern society, lithium-ion batteries (LIBs) have been considered to be one of the most promise environment-friendly power source for portable electronic devices, due to their high energy density and lower cost [1–7]. However, there are still remaining challenges associated with the larger-scale application for LIBs [8]. Thereinto, graphite as the most common commercial electrode is limited by its relatively low theoretical capacity (372 mAh $g^{-1}$) [9], and many researches have been carried out on seeking various anode materials as substitute. Specifically, ternary metal oxides ($AB_2O_4$; A, B: Mn, Ni, Cu, Zn, Fe, Co, etc.) with spinel structure exhibit favorable electrochemical capacity [10–13]. Among these materials, $ZnMn_2O_4$ is particularly attractive because of its high abundance, low cost, low toxicity and low operating potential (average discharging and charging voltages of 0.5 V and 1.2 V, respectively), comparing with Co-based or Cu-based oxides [14–19]. Remarkably, the lithium insertion process of $ZnMn_2O_4$ involves multistep reactions as shown below, i.e. conversion reactions (1, 2, 4) and alloying (3), which leads to a high energy density (784 mAh $g^{-1}$) [19–24].

$$ZnMn_2O_4 + 8Li^+ + 8e^- \rightarrow Zn + 2Mn + 4Li_2O \quad (1)$$

$$2Mn + 2Li_2O \leftrightarrow 2MnO + 4Li^+ + 4e^- \quad (2)$$

$$Zn + Li^+ + e^- \rightarrow LiZn \quad (3)$$

$$Zn + Li_2O \leftrightarrow ZnO + 2Li^+ + 2e^- \quad (4)$$

However, similar to other transition metal oxide electrodes, $ZnMn_2O_4$ has also suffered the disadvantages of low electrical conductivity and large volume change during the charge-discharge process. In this regard, many works have been conducted focusing on the design of various nanostructured materials, such as nanoflowers [25], nanospheres [20], and nanorods [26,27], to buffer the volume change of $ZnMn_2O_4$ and shorten the distance for ion and electron transport, so that to improve the electrochemical performance of $ZnMn_2O_4$-based materials as LIBs electrode. More

* Corresponding author. Department of Materials Science, Fudan University, Shanghai 200433, China.
*E-mail address:* yuxuebin@fudan.edu.cn (X. Yu).

https://doi.org/10.1016/j.electacta.2018.03.107
0013-4686/

recently, further achievements have been involved in designing composites that contain nanostructured $ZnMn_2O_4$ and conductive carbonaceous materials, taking advantage of the synergistic effect between active materials and carbonaceous materials [28,29]. Yin et al. anchored $ZnMn_2O_4$ nanocrystals in three-dimensional (3D) porous carbon aerogel (CA) [10]. Benefiting from the enormous interfacial surface area, connected 3D framework and abundant porosity of CA, $ZnMn_2O_4$/CA displayed a high capacity of 833 mAh $g^{-1}$ after 50 cycles at 100 mA $g^{-1}$ and 440 mAh $g^{-1}$ at 2000 mA $g^{-1}$. Furthermore, T. Zhang et al. employed hybrid inorganic/ordered mesoporous carbon (CMK3) to generate 2D-on-3D architecture, which provides abundant interfaces and electronic/ionic pathways for $ZnMn_2O_4$ nanosheets, leading to a high reversible capacity of 997 mAh $g^{-1}$ at 100 mA $g^{-1}$ after 100 cycles and a good rate capability with 693 mAh $g^{-1}$ at 2 A $g^{-1}$ [18]. Besides, it has been verified that graphene, one of the excellent carbonaceous materials, is also beneficial to modify the electrode materials, due to its high conductivity, high mechanical strength and high chemical stability [30–32]. Zheng et al. wrapped graphene oxide (GO) on the $ZnMn_2O_4$ nanofibers via a facile bottom-up approach. As a result, capabilities of 707 mAh $g^{-1}$ at 100 mA $g^{-1}$ over 50 cycles were achieved [33]. Cai et al. also reported a novel graphene-wrapped $ZnMn_2O_4$ porous spheres electrode that delivers a specific capacity of 926.4 mAh $g^{-1}$ after 100 cycles at 200 mA $g^{-1}$ and a high rate capacity of 560.8 mAh $g^{-1}$ at 1200 mA $g^{-1}$ [34].

In this work, we propose a facile approach to combine 3D reduced graphene oxide (rGO) wrapped carbon nanofibers (CNFs) and $ZnMn_2O_4$ nanoparticles to form a continuous-network-structured nanocomposite ($ZnMn_2O_4$@rGO-CNFs) by one-step electrospinning method. Firstly, the highly connective 1D nanofibers is in favor of electrical conductivity and the convenience of ion transport. Secondly, porous CNFs can play as a great buffer to accommodate the volume change during Li-ion insertion/extraction, as well as provide intercalation lithium sites. Finally, the uniformly package of rGO can not only increase electrical conductivity, but also avoid the pulverization of CNFs, ensuring a structural integrity. As expected, this unique structured nanocomposite exhibits a stable discharge capacity of 1142 mAh $g^{-1}$ (at 100 mA $g^{-1}$) after 100 cycles, and a capacity of 659 mAh $g^{-1}$ after 1000 cycles can be retained at a large current density of 2000 mA $g^{-1}$.

## 2. Experimental section

### 2.1. Materials synthesis

In order to synthesize $ZnMn_2O_4$@rGO-CNFs, a two-step process, including a simple one-step electrospinning process and an annealing process, was adopted. At first, GO (4%, 10%, 16% in term of PVA weight, corresponding to 20, 50, 80 mg dry GO weight) was mixed with Poly (vinyl alcohol) (PVA, 0.5 g, Alfa Aesar, Mv = 88 000), which was dissolved in deionized water (5 mL) and stirred in a water bath at 80 °C for 12 h to make a homogeneous PVA solution after 2 h ultrasonic treatment. After cooling down to room temperature, $Mn(CH_3COO)_2 \cdot 4H_2O$ (0.4 mmol, Sigma) and $Zn(CH_3COO)_2 \cdot 2H_2O$ (0.2 mmol, Sigma) were then added and vigorously stirred for 3 h to make a homogeneous precursor solution. The resultant spinning dope was poured into a syringe equipped with an 18-gauge blunt-tip stainless steel needle. The flow rate of solution was approximately 200 μL $h^{-1}$, controlled by a syringe pump (Longer, TJP-3A, China), During the electrospinning process, the needle and a collector plate were connected to a high-voltage generator. In this case, a voltage of 20 kV was applied between the cathode (metal collector plate) and the anode (needle) with a collection distance of 12 cm. The whole experiment was conducted in an extremely dry environment. The as-collected fibers were first dewatered at a temperature of 80 °C under dynamic vacuum for 12 h. Then the fibers were calcined at 250 °C for 6 h with a heating rate of 2 °C $min^{-1}$ in air and sintered at 550 °C with a temperature ramp rate of 5 °C $min^{-1}$ under dynamic $N_2$ atmosphere for 3 h to obtain the $ZnMn_2O_4$@rGO-CNFs. The synthetic process of $ZnMn_2O_4$-CNFs was similarly, without GO in the precursor solution.

### 2.2. Characterizations

The composition of powdered samples was investigated on an X-ray diffractometer (XRD; D8 Advance, Bruker AXS) with Cu Kα radiation at 50 kV and 30 mA. The chemical composition and valences of ZnMn2O4@rGO-CNFs were subsequently investigated by X-ray photoelectron spectroscopy (XPS). Fourier transform infrared (FTIR) spectra were collected at room temperature by using a FTIR-650 spectrometer (Tianjin Gangdong) at a resolution of 4 $cm^{-1}$. The morphology, microstructure, and elemental distribution were analyzed on a JEOL JEM-2100 F transmission electron microscope (TEM) and a Shimadzu JEOL 7500 F A scanning electron microscope (SEM). For the TEM measurements, the samples were dispersed in dried acetone solvent by ultrasonic treatment, and then spread on a copper grid. For SEM measurements, the samples were dispersed on electrically conducting adhesive tape. All the samples in the glove box were rapidly transferred into the equipment, which was filled with $N_2$, and then they were diverted into the chambers for TEM and SEM measurements as soon as possible. The distribution

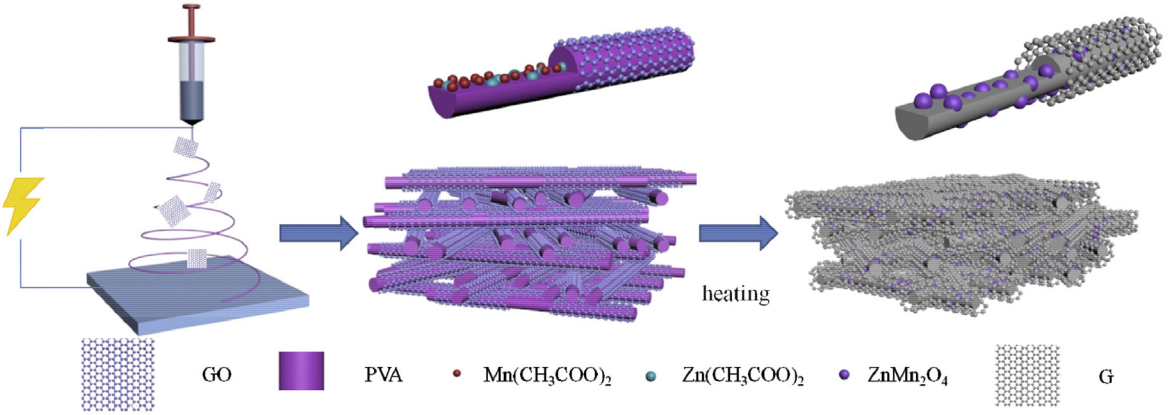


**Fig. 1.** Schematic illustration of the formation process for $ZnMn_2O_4$@rGO-CNFs composite.

of elemental Mn, Zn and O in the samples was detected with an energy-dispersive X-ray spectrometer (EDS) attached to the TEM. Thermal property measurements were performed by thermogravimetric analysis (TGA; STA 409C) with a heating rate of 10 °C $min^{-1}$ under air.

### 2.3. Electrochemical measurements

Electrochemical measurements were performed using coin type 2032 cells. The $ZnMn_2O_4$@rGO-CNFs and $ZnMn_2O_4$-CNFs networks were directly used as binder-free anodes. The electrolyte was made up of a mixture of 1 M $LiPF_6$ in fluoroethylene carbonate/dimethyl carbonate (1:1 in mass). The cells were assembled in an argon-filled glovebox. The galvanostatic charge and discharge measurements were performed on a LAND-CT2001C test system within the voltage cutoff window of 0.001–3 V (vs Li+/Li). Electrochemical impedance spectroscopy (EIS) and cyclic voltammetry (CV) was measured on an Autolab PGSTAT302 N electrochemical workstation at a scan rate of 0.1 mV $s^{-1}$.

## 3. Results and discussion

As shown in Fig. 1, the synthesis process of $ZnMn_2O_4$@rGO-CNFs is schematically displayed. Specifically, the graphene oxide (GO) wrapped polymeric nanofibers, containing the metal precursors, were first produced by electrospinning. Subsequently, the dried

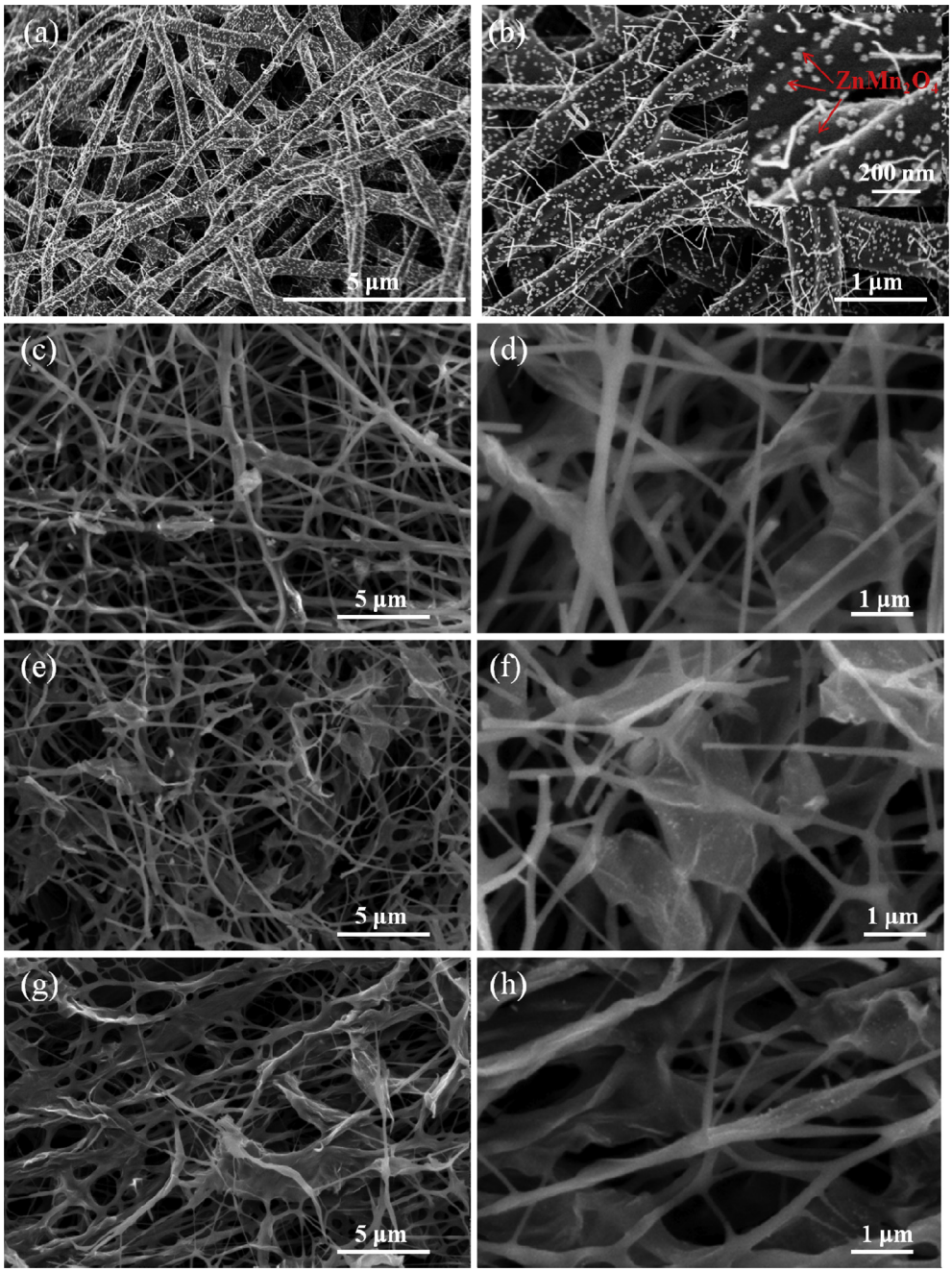


**Fig. 2.** SEM images of $ZnMn_2O_4$@rGO-CNFs with various GO addition. (a, b) Without GO, (c, d) 4% GO, (e, f) 10% GO and (g, h) 16% GO. The inset of (b) shows an enlarged image of $ZnMn_2O_4$-CNFs.

nanofibers were annealed in air at 250 °C for 6 h. During this process, some oxygen-containing functional groups of GO were thermally decomposed, while PVA started to decompose, which guaranteed a lower carbon yield of the final fibers (Fig. S1). The transformation from GO to rGO were caused by the reduction between GO and amorphous carbon generated from PVA in the following carbonization process in flowing $N_2$. And then, Mn ion and Zn ion react with oxygen functional groups from rGO and PVA at high temperature, leading to the generation of $ZnMn_2O_4$. At the same time, amorphous carbon was derived from PVA, which could act as a separator to prevent the $ZnMn_2O_4$ nanocrystals from growing into larger particles. The digital photos of the dried GO/$Mn(CH_3COO)_2$/PVA and the obtained $ZnMn_2O_4$@rGO-CNFs films (Fig. S2) displayed that the $ZnMn_2O_4$@rGO-CNFs film with a diameter of 1.5 cm.

By scanning electron microscopy (SEM) and transmission electron microscopy (TEM) coupled with energy-dispersive X-ray spectroscopy (EDS), the morphology and nanoarchitecture of $ZnMn_2O_4$@rGO-CNFs were characterized. As illustrated in Fig. 2, the composite obtained from various GO/PVA ratios showed different structures. For the sample without GO addition, the carbonized fibers showed an average diameter of ~350 nm, and $ZnMn_2O_4$ were grown largely up to ~50 nm on the surface of the CNFs (Fig. 2a and b). With the introduction of 4% GO (Fig. 2c and d), the diameter of the CNFs was decreased to around 200 nm and a few of them were wrapped by rGO. When the GO amount was increased to 10%, much more rGO sheets were covered on the CNFs with the formation of araneose structure (Fig. 2e and f). Further increasing the GO/PVA ratio to 16% (Fig. 2g, h), a continuous and interconnected belt-like structures were piled up, with the massive rGO sheets unfolded along the CNFs, indicating a thoroughly encapsulation of CNFs by rGO. The smoothing surfaces of $ZnMn_2O_4$@rGO-CNFs demonstrate that the $ZnMn_2O_4$ crystals were controlled in small size. The result highlights the important role of rGO in hindering the in-situ growth of $ZnMn_2O_4$ NPs during the calcination process. Besides, with the increase of the GO amount for $ZnMn_2O_4$@rGO-CNFs, the thermal stability of these composites became better and the content of $ZnMn_2O_4$ in these composites declined slightly (Fig. S3).

The TEM images of $ZnMn_2O_4$@rGO-CNFs-16% further verify that the CNFs networks were interconnected by rGO, and amorphous carbon nanofibers were wrapped or covered by rGO (Fig. 3a–c). It can be clearly observed that the $ZnMn_2O_4$ NPs with particle sizes ranging from 5 to 20 nm were uniformly encapsulated in these CNFs. The high-resolution TEM (HRTEM) image of $ZnMn_2O_4$@rGO-CNFs displays clear lattice fringes with interplanar spacing of 0.176 nm, 0.202 nm and 0.271 nm, corresponding to the (105), (220) and (103) planes of $ZnMn_2O_4$, respectively. In addition, obvious lattice fringes of graphene can be observed on the fiber edge, indicating that the amorphous carbon fibers were wrapped by the graphene successfully. Furthermore, EDS analysis (Fig. 3g–i) demonstrates that the element maps of Zn, Mn, and O matched very well with the shape of the as-prepared $ZnMn_2O_4$@rGO-CNFs-16% sample, suggesting the well-distributed $ZnMn_2O_4$ nanocrystals in the CNFs.

The as-prepared samples were further analyzed by X-ray diffraction (XRD). As shown in Fig. 4, all the diffraction peaks of

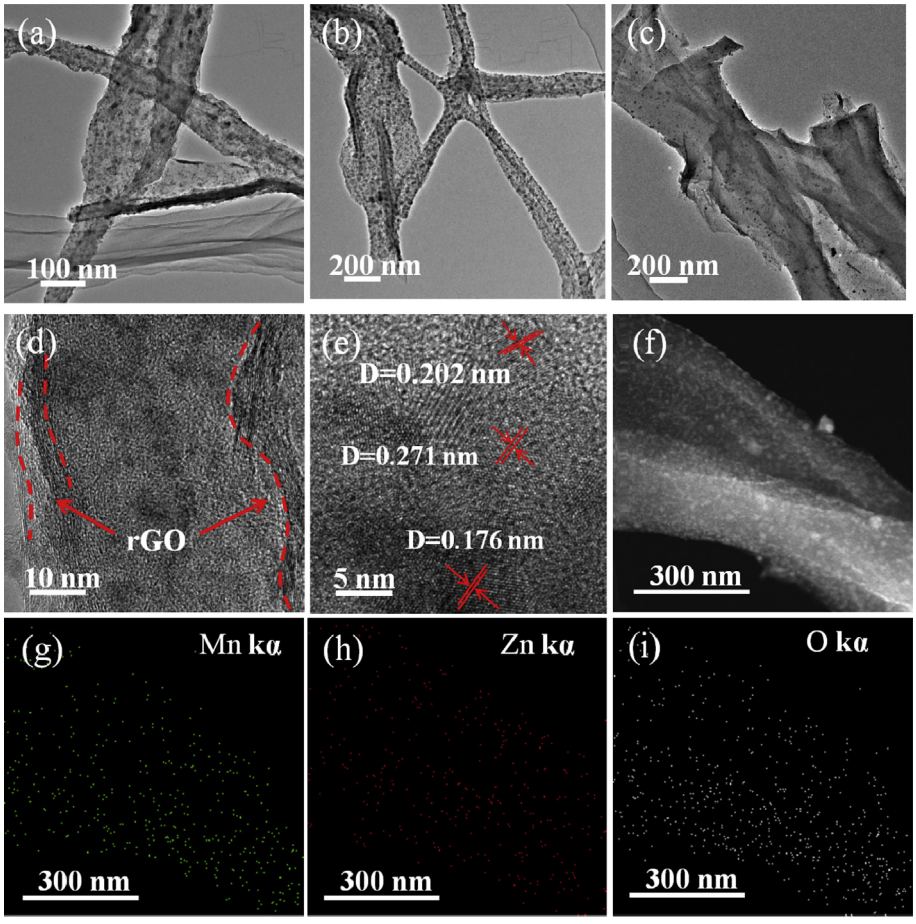


**Fig. 3.** TEM images (a, b, c) and HRTEM images (d, e) of $ZnMn_2O_4$@rGO-CNFs-16%, and the corresponding EDS maps of (g) Mn, (h) Mn, and (i) O elements for image (f).

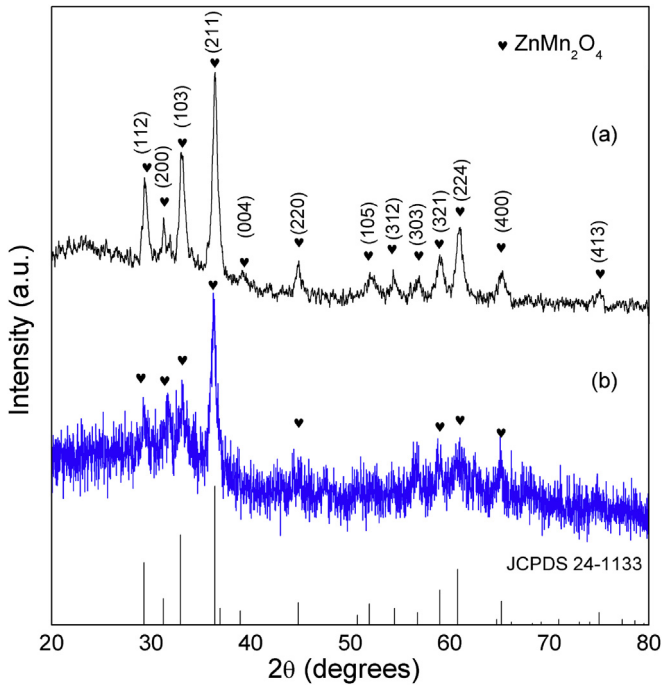


**Fig. 4.** X-ray diffraction (XRD) patterns of (a) $ZnMn_2O_4$-CNFs and (b) $ZnMn_2O_4$@rGO-CNFs-16%.

both $ZnMn_2O_4$-CNFs and $ZnMn_2O_4$@rGO-CNFs-16% could be ascribed to the $ZnMn_2O_4$ (JCPDS 24-1133) phase, which confirms the formation of crystallite $ZnMn_2O_4$ after the heating process. XRD pattern of the as-prepared $ZnMn_2O_4$-CNFs showed the obvious typical peaks belonging to $ZnMn_2O_4$. By comparison, only weak and broad peaks of the $ZnMn_2O_4$ phase were presented in the $ZnMn_2O_4$@rGO-CNFs-16% except the diffraction peak indexed to the (211) planes of the $ZnMn_2O_4$ phase. The difference between the two samples is due to the fact that the $ZnMn_2O_4$ NPs in $ZnMn_2O_4$@rGO-CNFs were embedded in the CNFs and the rGO cladding layers restricted the growth of NPs, which is in accordance with the SEM and TEM results.

In the X-ray photoelectron spectroscopy (XPS) spectra (Fig. 5), the characteristic peaks of Zn, Mn, C, and O can be clearly observed. The two obvious peaks at around 643.8 eV and 655.4 eV can be assigned to the Mn 2p3/2 and Mn 2p1/2, respectively, in Mn 2p spectrum (Fig. 5b). The binding energy separation between these two peaks is 11.8 eV, which is in accordance with that of $ZnMn_2O_4$ [8,46]. In Zn 2p spectrum (Fig. 5c), there are two peaks at the blinding energies of 1022.0 and 1046.2 eV, corresponding to Zn 2p3/2 and Zn 2p1/2 of $Zn^{2+}$, respectively, indicating the oxidation state of Zn in the $ZnMn_2O_4$ [21,35–38]. Two obvious peaks at 284.68, and 285.7 eV can be observed in high-resolution XPS spectrum of C1s for the $ZnMn_2O_4$@rGO-CNFs (Fig. 5d), matching to the C-C sp2, and C-C sp3, respectively. The results indicate the high graphitic degree of the CNFs and the reduction reaction of GO. Besides, there is a slight O-C=O peak (288.78 eV) linked to porous CNFs and $ZnMn_2O_4$ in the spectrum [39–41]. Fig. S4 showed the Fourier transform infrared (FTIR) results of $ZnMn_2O_4$@rGO-CNFs compared with GO. The strong peaks present at wavenumbers of 1626, 1718, and 3423 $cm^{-1}$ are assigned to the C=C, C=O and C-OH stretching vibration of GO, respectively, while there are only two modest fluctuations at around 1626, and 3423 $cm^{-1}$ for $ZnMn_2O_4$@rGO-CNFs. It is evident that the GO was reduced to rGO successfully for the $ZnMn_2O_4$@rGO-CNFs sample, which is consistent with the de-convoluted XPS results.

The electrochemical performance of $ZnMn_2O_4$@rGO-CNFs as binder-free anode material for LIBs was evaluated by cyclic

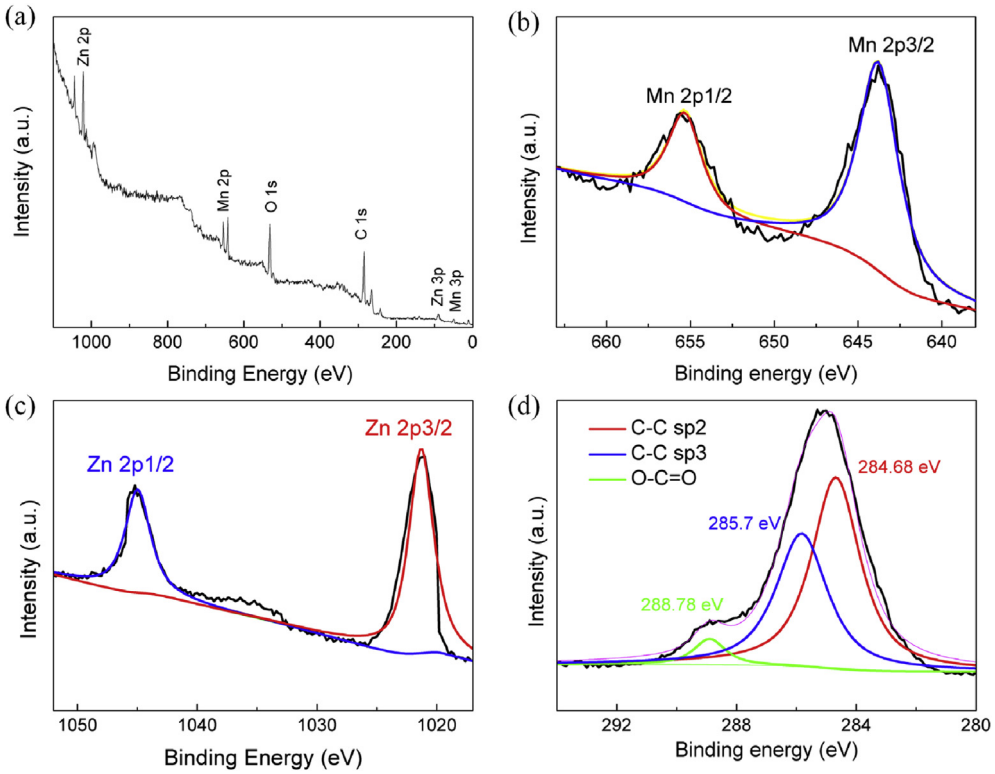


**Fig. 5.** a) Full XPS profile, b) high-resolution Mn2p, c) Zn2p and d) C1s spectrum of the as-synthesized $ZnMn_2O_4$@rGO-CNFs-16%.

voltammograms (CV), with a cut-off voltage of 0.01–3.00 V versus $Li/Li^+$. As illustrated in Fig. 6a, a weak cathodic peak observed at 1.1 V in the initial cycle is attributed to the reduction of $Mn^{3+}$ to $Mn^{2+}$, while another intensive reduction peak (~0.12 V) might arise from the reduction process of $Mn^{2+}$ and $Zn^{2+}$ to $Mn^0$ and $Zn^0$, as well as the alloying process of Zn with Li, coupled with the formation of $Li_2O$. In addition, with the cycle number increasing, the reduction peaks shifted to 0.45 V with significantly lessened intensity, suggesting the irreversible phase transformation, the irreversible reduction of electrolytes and the generation of a solid electrolyte interphase (SEI) film in the initial cycle. A broad anodic peak located at ≈1.25 V during the reverse scan corresponds to the oxidation of $Zn^0$ to $Zn^{2+}$ and $Mn^0$ to $Mn^{2+}$, accompanied by the decomposition of $Li_2O$ [10,37,44,45]. By contrast, there is only one reduction peak at 0.63 V for the rGO electrode (Fig. S5) in the first cycle due to the formation of SEI. It is remarkable that the almost overlapping CV curves of the subsequent cycles index a stable reversibility of the $ZnMn_2O_4$@rGO-CNFs during lithium-ion intercalation and deintercalation process. Meanwhile, the correlative plateau regions at approximately 0.45 V and 1.1 V in the initial five charge–discharge profiles of the $ZnMn_2O_4$@rGO-CNFs (Fig. 6b) are in good accordance with the results of the above CV analysis. Notably, the low charge potential could be beneficial to a higher working voltage when serving as electrode in a full cell, leading to a higher energy density. The $ZnMn_2O_4$@rGO-CNFs-16% electrode delivered the initial discharge and charge capacity of 2214 and 1343 mAh $g^{-1}$ at 100 mA $g^{-1}$, respectively, corresponding to a 60.6% coulombic efficiency (CE). The large irreversible capacity in the first

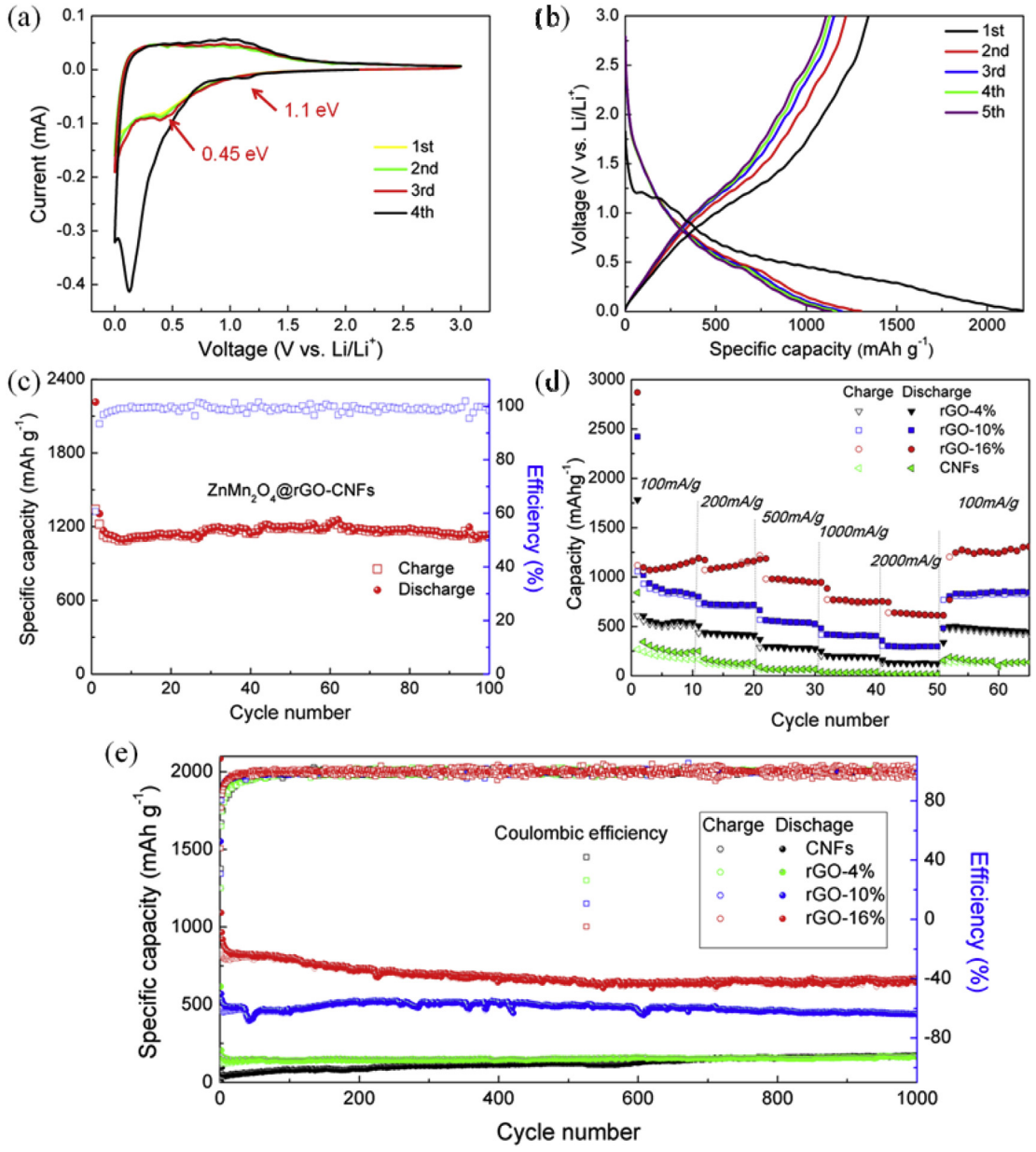


**Fig. 6.** Electrochemical performance of the $ZnMn_2O_4$@rGO-CNFs electrode in LIBs. (a) Cyclic voltammograms for the initial four cycles at a scanning rate of 0.2 mV $s^{-1}$. (b) Galvanostatic discharge-charge profiles for initial five cycles at a current density of 100 mA $g^{-1}$. (c) Cycling performance at a current density of 100 mA $g^{-1}$ of the $ZnMn_2O_4$@rGO-CNFs-16% electrode. (d) Rate performance at different current densities from 100 mA $g^{-1}$ to 2000 mA $g^{-1}$, (e) Cycling performance at a current density of 2000 mA $g^{-1}$ of the $ZnMn_2O_4$@rGO-CNFs-4%/10%/16% electrode, with $ZnMn_2O_4$-CNFs included for comparison.

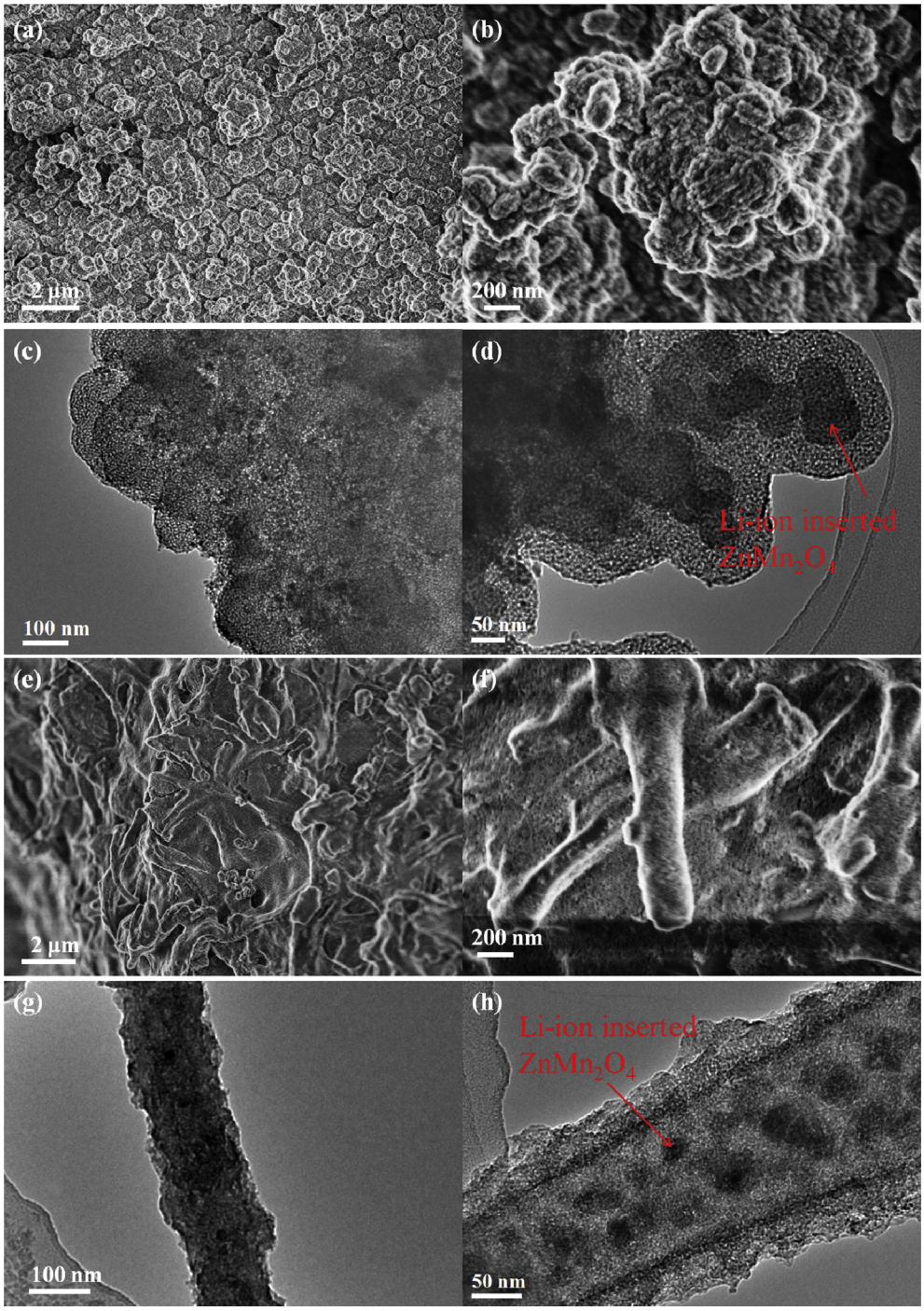


**Fig. 7.** SEM images of $ZnMn_2O_4$-CNFs (a, b) and $ZnMn_2O_4$@rGO-CNFs-16% (e, f); TEM images of $ZnMn_2O_4$-CNFs (c, d) and $ZnMn_2O_4$@rGO-CNFs-16% (g, h) after 500 discharge/charge cycles at 2000 mA $g^{-1}$.

cycle could be attributed to the formation of solid electrolyte interphase (SEI) film or other side reactions. The CE significantly increased to 93.4% for the second cycle and remained at nearly 100% after the 10th cycle, indicating a favorable reversibility of the electrode. Remarkably, the reversible capacity leveled off at around 1100 mAh $g^{-1}$ at the rate of 100 mA $g^{-1}$, which remained at 1142 mAh $g^{-1}$ after 100 cycles (Fig. 6c). It should be mentioned that due to the synergistic effect between $ZnMn_2O_4$ and carbon/rGO, the capacity of $ZnMn_2O_4$@rGO-CNFs-16% was even higher than the theoretical value of $ZnMn_2O_4$. Besides, the tendency of the capacity change was flat, without obvious fluctuation. This is attributed to the rapid activation process and the stable reaction in the electrode.

In addition to the specific capacity and cycling stability, another critical evaluation index, the rate performance of the as-synthesized $ZnMn_2O_4$@rGO-CNFs, was investigated with the $ZnMn_2O_4$-CNFs for comparison. The rate capability and the cycle performance at different current densities ranging from 100 to 2000 mA $g^{-1}$ are displayed in Fig. 6d. With the current density increased from 100 to, 200, 500, 1000, and 2000 mA $g^{-1}$, the discharge specific capacity of the 10th cycle for $ZnMn_2O_4$@rGO-

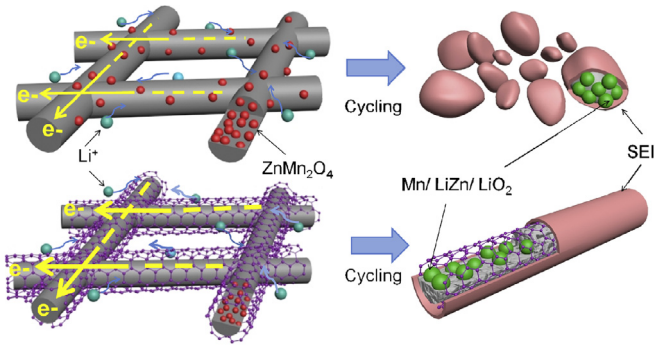


**Fig. 8.** Schematic illustration of the cycling process of $ZnMn_2O_4$-CNFs and $ZnMn_2O_4$@rGO-CNFs electrode.

CNFs-4% was 534, 413, 272, 192 and 124 mAh $g^{-1}$, respectively. For the sample with a GO/PVA ratio up to 16%, the discharge specific capacity could reach to 1167, 1164, 946, 750 and 612 mAh $g^{-1}$, respectively. When the current density was recovered to 100 mAh $g^{-1}$, the specific capacity could enhance to 1244 mAh $g^{-1}$ further, implying a very stable cycling performance. Clearly, with the increase of the GO amount for $ZnMn_2O_4$@rGO-CNFs, both of specific capacity and rate performance were improved greatly in term of the similar $ZnMn_2O_4$ content. This can be attributed to the structural transformation and higher conductivity of the samples with GO addition. The $ZnMn_2O_4$@rGO-CNFs- 4%/10%/16% electrodes were tested at 2000 mA $g^{-1}$ to further illustrate the electrochemical performance at high current density. All of the three electrodes remained stable, with average variation of 0.027%, 0.004% and 0.019% per cycle from the 2nd cycle to 1000th cycle, indicating the excellent cycle stability of $ZnMn_2O_4$@rGO-CNFs even at a high current density. By comparison, the capacity of $ZnMn_2O_4$-CNFs was lower than 100 mAh $g^{-1}$ in the first 200 cycle. Moreover, the $ZnMn_2O_4$@rGO-CNFs-4%/10%/16% exhibited reversible capacity of 165, 439 and 659 mAh $g^{-1}$, respectively, after 1000 cycles at a high current density of 2000 mA $g^{-1}$ (Fig. 6e). Compared with previously reported manganese oxide/carbonaceous hybrid materials (Table S1), the $ZnMn_2O_4$@rGO-CNFs electrode shows competitive reversible capacity. The SEM and TEM images of the $ZnMn_2O_4$-CNFs and $ZnMn_2O_4$@rGO-CNFs-16% electrode cycled after 500 times at 2000 mA $g^{-1}$ are compared in Fig. 7. It can be seen that even after a prolonged cycling of 500 times, the fiber structure of $ZnMn_2O_4$@rGO-CNFs-16% can be well maintained and the average size of Li-ion inserted nanoparticles is still ~25 nm, suggesting the high stability of $ZnMn_2O_4$@rGO-CNFs structure upon cycling. The SEI layers coated on the surface of nanofibers homogenously due to the protection of rGO layers. By contrast, the original fiber structure of $ZnMn_2O_4$-CNFs collapsed with size of Li-ion inserted nanoparticles over 50 nm, which were attributed to the stress and strain induced by the repeated discharge and charge process. The EIS measurements were performed to further investigate the remarkable effect of rGO and the structure of the $ZnMn_2O_4$@rGO-CNFs-16%. EIS plots (Fig. S6a.) reveal that the diameter of the semicircle for electrode become smaller with the increase of rGO, indicating that the introduction of rGO sheets leads to the higher electrical conductivity. It is clearly that the $ZnMn_2O_4$@rGO-CNFs-16% electrode after 10 cycles at 500 mA $g^{-1}$ exhibits a smaller semicircle diameter (Fig. S6b.), demonstrating a lower charge transfer impedance, which is attributed to the electrode-electrolyte activation in the initial cycles.

Therefore, the excellent electrochemical performance of $ZnMn_2O_4$@rGO-CNFs is mainly ascribed to its unique structural features (Fig. 8). First, the continuous and connective one-dimensional morphology, high surface area, and high porosity of nanofibers decrease the length of $Li^+$ diffusion pathways, and increase the contact of electrolyte and pores, leading to the improved capability and kinetic properties [42,43]. Second, the small active $ZnMn_2O_4$ NPs are homogeneously distributed in the carbon nanofibers, leading to a higher use ratio and the reduction of aggregation of active materials during electrochemical processes. More importantly, the mechanical property of the wrapped rGO is strong enough to restrict the volume expansion of $ZnMn_2O_4$ and the pulverization of CNFs during long-term lithiation processes, leading to a higher cycling stability.

## 4. Conclusion

In conclusion, we have successfully fabricated a novel anode material, $ZnMn_2O_4$@rGO-CNFs, via a facile electrospinning technique and followed heating treatment. In $ZnMn_2O_4$@rGO-CNFs, the $ZnMn_2O_4$ NPs were homogeneously distributed in the reduced graphene wrapped porous carbon nanofibers networks. The unique structural features of $ZnMn_2O_4$@rGO-CNFs not only provide more active sites for lithium insertions, but also shorten the ion/electron diffusion distance. More importantly, the rGO sheets can effectively protect the CNFs from pulverization due to the volume expansion of $ZnMn_2O_4$ NPs during long-term cycling process, and thus maintaining a good electrical conductivity. As a result, the $ZnMn_2O_4$@rGO-CNFs electrode exhibited excellent electrochemical performances with high capacity, stable cycling and favorable high rate capability. This study offers a more flexible method for designing electrode materials for LIBs with high and stable performance.

## Acknowledgements

This work was partially supported by the National Key Research and Development Program of China (2017YFA0204600), the Key Research and Development Plan Project of Zhejiang Province (No.2018C01036), the National Science Fund for Distinguished Young Scholars (51625102), the National Natural Science Foundation of China (51471053) and the Science and Technology Commission of Shanghai Municipality (17XD1400700).

## Appendix A. Supplementary data

Supplementary data related to this article can be found at https://doi.org/10.1016/j.electacta.2018.03.107.

## References

[1] B. Scrosati, J. Garche, J. Power Sources 195 (2010) 2419–2430.
[2] M. Park, X. Zhang, M. Chung, G.B. Less, A.M. Sastry, J. Power Sources 195 (2010) 7904–7929.
[3] S.P. Esra, S. Elena, S. Bálint, K. Ali, J. Power Sources 300 (2015) 199–215.
[4] N. Armaroli, V. Balzani, Energy Environ. Sci. 4 (2011) 3193–3222.
[5] Y. Xu, Z. Lin, X. Zhong, B. Papandrea, Y. Huang, X. Duan, Angew. Chem. Int. Ed. 54 (2015) 5345–5350.
[6] V. Etacheri, R. Marom, R. Elazari, G. Salitra, D. Aurbach, Energy Environ. Sci. 4 (2011) 3243–3262.
[7] M.V. Reddy, G.V. Subba Rao, B.V.R. Chowdari, Chem. Rev. 113 (2013) 5364–5457.
[8] J.G. Kim, S.H. Lee, Y. Kim, W.B. Kim, ACS Appl. Mater. Interfaces 5 (2013) 11321–11328.
[9] L. Ji, Z. Lin, M. Alcoutlabi, X. Zhang, Energy Environ. Sci. 4 (2011) 2682–2699.
[10] L. Yin, Z. Zhang, Z. Li, F. Hao, Q. Li, C. Wang, R. Fa, Y. Qi, Adv. Funct. Mater. 24 (2014) 4176–4185.
[11] M. Bijelić, X. Liu, Q. Sun, A.B. Djurišić, M.H. Xie, A.M.C. Ng, C. Suchomski, I. Djerdj, Ž. Skokoa, J. Popović, J. Mater. Chem. A 3 (2015) 14759–14767.
[12] K. Cao, T. Jin, Li Yang, L. Jiao, Mater. Chem. Front 1 (2017) 2213–2242.
[13] Z.-J. Jiang, S. Cheng, H. Rong, Z. Jiang, J. Huang, J. Mater. Chem. A 5 (2017) 23641–23650.
[14] Y. Yang, Y. Zhao, L. Xiao, L. Zhang, Electrochem. Commun. 10 (2008)

1117–1120.
[15] N. Wang, X. Ma, H. Xu, L. Chen, J. Yue, F. Niu, J. Yang, Y. Qian, Nanomater. Energy 6 (2014) 193–199.
[16] G.Q. Zhang, L. Yu, H.B. Wu, H.E. Hoster, X.W. Lou, Adv. Mater. 24 (2012) 4609–4613.
[17] J. Zhao, F. Wang, P. Su, M. Li, J. Chen, Q. Yang, C. Li, J. Mater. Chem. 22 (2012) 13328–13333.
[18] T. Zhang, H. Qiu, M. Zhang, Z. Fang, X. Zhao, L. Wang, et al., Carbon 123 (2017) 717–725.
[19] X. Chen, Y. Zhang, H. Lin, P. Xia, X. Cai, X. Li, X. Li, J. Power Sources 312 (2016) 137–145.
[20] Y. Liu, J. Ba, X. Ma, J. Li, S. Xiong, J. Mater. Chem. A 2 (2014) 14236–14244.
[21] C. Yuan, L. Zhang, L. Hou, L. Zhou, G. Pang, L. Lian, Chem. Eur J. 21 (2015) 1262–1268.
[22] Z.C. Bai, N. Fan, C.H. Sun, Z.C. Ju, C.L. Guo, J. Yang, Y.T. Qian, Nanoscale 5 (2013) 2442–2447.
[23] F.M. Courtel, H. Duncan, Y. Abu-Lebdeh, I.J. Davidson, J. Mater. Chem. 21 (2011) 10206–10218.
[24] J. Zeng, Y. Ren, S. Wang, Y. Hao, H. Wu, S. Zhang, Y. Xing, Inorg. Chem. Front 4 (2017) 1730–1736.
[25] L. Xiao, Y. Yang, J. Yin, Q. Li, L. Zhang, J. Power Sources 194 (2009) 1089–1093.
[26] P.F. Teh, Y. Sharma, Y.W. Ko, S.S. Pramana, M. Srinivasan, RSC Adv. 3 (2013) 2812–2821.
[27] P. Zhang, X. Li, Q. Zhao, S. Liu, Nanoscale Res. Lett. 6 (2011) 1–8.
[28] Y. Deng, L. Wan, Y. Xie, X. Qin, G. Chen, RSC Adv. 4 (2014) 23914–23935.
[29] Q. Sun, M. Bijelić, A. B Djurišić, C. Suchomski, X. Liu, M. Xie, A.M.C. Ng, H.K. Li, K. Shih, S. Burazer, Ž. Skoko, I. Djerdj, J. Popović, Nanotechnology 28 (2017), 455401.
[30] A.K. Geim, Science 324 (2009) 1530–1534.
[31] S.B. Yang, X.L. Feng, S. Ivanovici, K. Mullen, Angew. Chem. Int. Ed. 49 (2010) 8408–8411.
[32] Z.L. Wang, D. Xu, Y. Huang, Z. Wu, L.M. Wang, X.B. Zhang, Chem. Commun. (J. Chem. Soc. Sect. D) 48 (2012) 976–978.
[33] Z.M. Zheng, Y.L. Cheng, X.B. Yan, R.T. Wang, P. Zhang, J. Mater. Chem. A 2 (2014) 149–154.
[34] D. Cai, D. Wang, H. Huang, X. Duan, B. Liu, L. Wang, Y. Liu, Q. Li, T. Wang, J. Mater. Chem. A 3 (2015) 11430–11436.
[35] X. Gu, J. Yue, L. Chen, S. Liu, H. Xu, J. Yang, Y. Qian, X. Zhao, J. Mater. Chem. A 3 (2015) 1037–1041.
[36] M. Zhong, D. Yang, C. Xie, Z. Zhang, Z. Zhou, X.-H. Bu, Small 12 (2016) 5564–5571.
[37] J. Yuan, C. Chen, Y. Hao, X. Zhang, R. Agrawal, W. Zhao, C. Wang, H. Yu, X. Zhu, Y. Yu, Z. Xiong, Y. Xie, J. Alloys. Compd. 696 (2017) 1174–1179.
[38] B. Fan, A. Hu, X. Chena, S. Zhang, Q. Tang, J. Wang, W. Deng, Z. Liua, K. Xiao, Electrochim. Acta 213 (2016) 37–45.
[39] R.M.N.M. Rathnayake, H.W.M.A.C. Wijayasinghe, H.M.T.G.A. Pitawa, M. Yoshimura, H.-H. Huang, Appl. Surf. Sci. 393 (2017) 309–315.
[40] C. Zhang, W. Lv, X. Xie, D. Tang, C. Liu, Q.-H. Yang, Carbon 62 (2013) 11–24.
[41] D.R. Dreyer, S. Park, C.W. Bielawski, R.S. Ruoff, Chem. Soc. Rev. 39 (2010) 228–240.
[42] V. Aravindan, J. Sundaramurthy, P.S. Kumar, Y.-S. Lee, S. Ramakrishna, S. Madhavi, Chem. Commun. (J. Chem. Soc. Sect. D) 51 (2015) 2225–2234.
[43] E.S. Pampal, E. Stojanovska, B. Simon, A. Kilic, J. Power Sources 300 (2015) 199–215.
[44] M.H. Alfaruqi, A.K. Rai, V. Mathew, J. Jo, J. Kim, Electrochim. Acta 151 (2015) 558–564.
[45] P. Li, J. Liu, Y. Liu, Y. Wang, Z. Li, W. Wu, Y. Wang, L. Yin, H. Xie, M. Wu, X. He, J. Qiu, Electrochim. Acta 180 (2015) 164–172.
[46] M.C. Biesinger, B.P. Payne, A.P. Grosvenor, L.W.M. Lau, A.R. Gerson, R.S.C. Smart, Appl. Surf. Sci. 257 (2011) 2717–2730.